JGR Solid Earth

Key Points:

- Multi-anvil press experiments in the system $MgSiO_3$-SiO_2 at 24 GPa located the eutectic at 53 mol% SiO_2 and 2750 K
- We build a thermodynamic model for MgO-SiO_2 based on the data and other constraints that allows extrapolation to the core-mantle boundary
- Based on melting curves of MgO and SiO_2 and their liquid interaction parameter, the model predicts eutectic temperatures and compositions

Correspondence to:

G. Steinle-Neumann,
g.steinle-neumann@uni-bayreuth.de

Lower Mantle Melting: Experiments and Thermodynamic Modeling in the System MgO-SiO₂

Jie Yao[1], Daniel J. Frost[1] , and Gerd Steinle-Neumann[1]

[1]Bayerisches Geoinstitut, Universität Bayreuth, Bayreuth, Germany

Abstract Characterizing and modeling melting relations in the system MgO-SiO_2 at lower mantle pressures rely on the location of the eutectic points for MgO-$MgSiO_3$ and $MgSiO_3$-SiO_2. While at an uppermost lower mantle pressure there is general consensus on the eutectic composition in the former, large discrepancies exist for $MgSiO_3$-SiO_2 from experiments in the diamond anvil cell, ab-initio simulations and models built on them. In order to address this discrepancy, we have performed multi-anvil press experiments at 24 GPa for $Mg_4Si_6O_{16}$ and $Mg_3Si_7O_{17}$ at temperatures of 2650 ± 100 K and 2750 ± 100 K. In the experiments at 2750 ± 100 K, we observe the presence of partial melt. The recovered $Mg_4Si_6O_{16}$ sample shows SiO_2 stishovite as the liquidus phase, and electron microprobe analysis of the quenched melt determines $X_{SiO_2} = 0.53 \pm 0.03$ as the eutectic composition. We fit a thermodynamic model to describe the melting relations in the MgO-SiO_2 system, and extrapolate to core-mantle boundary pressure. At 136 GPa, we predict that the eutectic points have moved further away from enstatite composition, and solidus temperatures remain similar for MgO-$MgSiO_3$ and $MgSiO_3$-SiO_2.

Plain Language Summary Melting of rock in the Earth's deep interior is an important process that has shaped its geological history, and continues to do so to date. However, melting processes at high pressure have not been fully characterized to date, and here we perform experiments that help to better describe models for it. We do so for compositions in the $MgSiO_3$-SiO_2 system that complement prior work for MgO-$MgSiO_3$; combined, these experiments put important constraints on melting for the most important chemical components in the Earth's mantle, MgO-SiO_2. We find that when silicate melts crystallize, they do form the dominant lowermost mantle mineral, $MgSiO_3$ bridgmanite, only for a limited composition range in terms of the SiO_2/MgO ratio; otherwise, MgO or SiO_2 form first, and generally at much higher temperatures. Melts in both the MgO-$MgSiO_3$ and $MgSiO_3$-SiO_2 systems become fully crystallized at very similar temperatures which suggests that a prior idea that the occurrence of partial melts in the Earth's deepest mantle is associated with different chemical composition does not hold if only the MgO-SiO_2 system is considered.

1. Introduction

Silicate melting has shaped the chemical and physical evolution of Earth's interior, from magma ocean formation during accretion (Elkins-Tanton et al., 2003; Elardo et al., 2011; Monteux et al., 2016; Wood & Halliday, 2005) to the continuous extraction of melt through plate tectonic processes. The latter is dominated by the ongoing formation of mid-ocean ridge basalt (MORB) from mantle peridotite (Kelemen et al., 1995). Melts may also form at the boundaries of the mantle transition zone (e.g., Revenaugh & Sipkin, 1994; Schmandt et al., 2014) and near the core-mantle boundary (CMB), where they serve as an explanation (e.g., Andrault et al., 2014; Labrosse et al., 2007) for the occurrence of seismic ultra-low velocity zones (ULVZ; Hernlund & Jellinek, 2010; Rost et al., 2005). Most deep melting processes are mitigated by the influence of volatile components (Dasgupta, 2018; Johnson et al., 2008), but despite volatile loss of slab material transported into Earth's deep interior (e.g., Chemia et al., 2015), dry melting may occur within the thermal boundary layer at the base of the mantle (Hirose et al., 1999).

Melting experiments on natural rocks (e.g., Andrault et al., 2014; Fiquet et al., 2010; Pradhan et al., 2015) at lower mantle (LM) pressure ($P \geq 24$ GPa) yield valuable insight on solidus and liquidus temperatures (T), but the complexity of composition, the small size of samples, especially in diamond anvil cell (DAC) experiments, and large thermal gradients make it difficult to identify the liquidus and solidus in a systematic way. Therefore, the consideration of simplified systems is required in high-P experiments in order to develop a thermodynamic description that can successively be built up by adding components, ideally combining well-controlled multi-anvil

Writing – original draft: Gerd Steinle-Neumann
Writing – review & editing: Daniel J. Frost

(MA) press and DAC experiments. The two-component MgO-SiO$_2$ system provides the basis of such a model, but has not yet been fully characterized.

Given a molar ratio MgO/SiO$_2$ ~ 1.15 or X_{SiO_2} = 0.47, with $X_{SiO_2} = \left(SiO_2/SiO_2 + MgO\right)$, for the bulk Earth (Dauphas et al., 2015) and X_{SiO_2} = 0.45 for the bulk silicate Earth (Palme & O'Neill, 2003), many experiments on melt relations in MgO-SiO$_2$ have focused on the MgO-MgSiO$_3$ subsystem (Liebske & Frost, 2012; Ohnishi et al., 2017). However, SiO$_2$-enriched reservoirs in the Earth, primarily associated with oceanic crust, have been considered as potential sources for partial melting near the CMB (Andrault et al., 2014; Nomura et al., 2014), and related to the observation of the ULVZ there (Thorne et al., 2019). The location of the eutectic in the Mg-SiO$_3$-SiO$_2$ system may further be directly relevant for the aubrite parent body in our solar system with X_{SiO_2} > 0.5 (Dauphas et al., 2015), and for rocky exoplanets as some of the stars in the Hypathia Catalog, taken as a proxy for potential planetary compositions, show X_{SiO_2} ~ 0.6 (Hinkel & Unterborn, 2018).

Experiments on melt relations in the MgO-SiO$_2$ system at lower mantle P were performed in the MA press by Liebske and Frost (2012), the DAC by Baron et al. (2017), Ohnishi et al. (2017), and Ozawa et al. (2018), modeled based on ab-initio simulations by de Koker et al. (2013), and thermodynamically described by Boukaré et al. (2015), Miyazaki and Korenaga (2019) and Belmonte et al. (2017). Bridgmanite is the phase at the liquidus in the vicinity of the enstatite composition, with two eutectics points bracketing its stability; this stability field has been found to expand with P.

At P = 24 – 25 GPa, the eutectic composition on the MgO-MgSiO$_3$ join is consistently determined as X_{SiO_2} = 0.43 ± 0.01 (Belmonte et al., 2017; Boukaré et al., 2015; de Koker et al., 2013; Liebske & Frost, 2012; Ohnishi et al., 2017; Ozawa et al., 2018) with some uncertainty in T, ranging from ~2700 K (Liebske & Frost, 2012) to ~2900 K (Boukaré et al., 2015). For MgSiO$_3$-SiO$_2$, de Koker et al. (2013) find X_{SiO_2} = 0.62 ± 0.01 at a eutectic temperature T_e, lower by 100–150 K than for MgO-MgSiO$_3$ at 24 GPa, while Belmonte et al. (2017) compute X_{SiO_2} = 0.51 at T_e ~ 2800 K, ~50 K higher than for the peridotite eutectic. Ozawa et al. (2018) determine X_{SiO_2} = 0.60 at P = 40 GPa in DAC experiments and extrapolate to X_{SiO_2} = 0.58 and T ~ 2500 K at P = 25 GPa, by contrast. However, to date melting relations for MgSiO$_3$-SiO$_2$ have not been studied in the MA press, although it provides better control of thermal gradients and allows more rigorous textural analysis of the larger sample compared to DAC experiments. Here we perform MA melting experiments at P = 24 GPa with Mg$_4$Si$_6$O$_{16}$ and Mg$_3$Si$_7$O$_{17}$ starting compositions, complementing the work by Liebske and Frost (2012).

2. Experimental and Analytical Methods

The synthesis of compositions along the MgSiO$_3$-SiO$_2$ join (Mg$_4$Si$_6$O$_{16}$ and Mg$_3$Si$_7$O$_{17}$) requires MgSiO$_3$ glass, for which analytical-grade MgO and SiO$_2$ powders (1 : 1 molar ratio) are mixed in ethanol, dried under infrared light, and ground to a fine powder. The mixture is melted in a Pt crucible for 30 minutes at 1650 °C and quenched by dropping the crucible into water. The MgSiO$_3$ glass is repeatedly ground to a fine powder in ethanol and then dried. Mg$_4$Si$_6$O$_{16}$ and Mg$_3$Si$_7$O$_{17}$ powders are prepared by mixing the ground enstatite glass with SiO$_2$ powder; they are stored under vacuum to prevent hydration.

We perform melting experiments using the 1,200 t Sumitomo MA press at Bayerisches Geoinstitut (Keppler & Frost, 2005). The sample powder is put in a Rhenium (Re) capsule (~2 mm in length and ~1 mm in diameter), closed with a Re foil disk on top and bottom, and inserted in a Cr$_2$O$_3$-doped MgO octahedron (7 mm edge length). A LaCrO$_3$ heater inside the octahedron is insulated from the Re capsule by a MgO sleeve (Figure S1 in Supporting Information S1). Cell assembly parts are stored in an oven at 1000°C for 12 hr to dehydrate prior to use. The octahedron is compressed by tungsten carbide anvils with 3 mm corner truncations (7/3 assembly). The assembly is compressed to P = 24 GPa, heated to the target T and kept there for 1 – 2 minutes. The run product is quenched by shutting off the power and slowly decompressed to ambient conditions over 16 h. We perform experiments without thermocouples and extrapolate the heating power-T relation, determined in an independent experiment at P = 24 GPa with the same setup to a power of 433 W (T = 2375 K) using W-Re wires as thermocouples, to 450 – 470 W applied here. To account for the P dependence of thermocouple electromotive force, we follow Nishihara et al. (2020) and add a correction to estimate the T of the experiments (Table 1), with an uncertainty of ± 100 K. Thermocouples tend to fail at the conditions explored (e.g., Liebske & Frost, 2012), and using power instead makes T conditions in the experiments far more reproducible.

Table 1
Experimental Run Conditions for the Multi-Anvil Press Experiments Performed in This Study at 24 GPa

Experiment	Power (W)	Temperature (K)	Initial composition	Phases	Liquid composition (mol %)	
					SiO$_2$	MgO
S7110	450	2650 ± 100	Mg$_4$Si$_6$O$_{16}$	st, brg	–	–
S7152	450	2650 ± 100	Mg$_3$Si$_7$O$_{17}$	st, brg	–	–
S7172	469	2750 ± 100	Mg$_3$Si$_7$O$_{17}$	st, brg, (liq)	–	–
S7238	470	2750 ± 100	Mg$_4$Si$_6$O$_{16}$	liq, st	53 ± 3	47 ± 2

Note. brg, bridgmanite; liq, liquid; st, stishovite.

Recovered sample chambers are mounted within epoxy parallel to the cylinder axis and then polished to the central section to observe phase relations along the thermal gradient, which is parallel to the furnace axis. The texture is analyzed with a LEO1530 scanning electron microscope (SEM) at acceleration voltage 15 – 20 kV and beam current 10 nA. Chemical compositions of the run products are determined using a JEOL JXA-8200 electron microprobe (EPMA) at acceleration voltage 15 – 20 kV with focused beam for mineral phases and a beam diameter of 30 µm. Counting times are 20 s on the peak and 10 s on the background for each element. Enstatite and orthoclase standards are used for Mg and Si calibration.
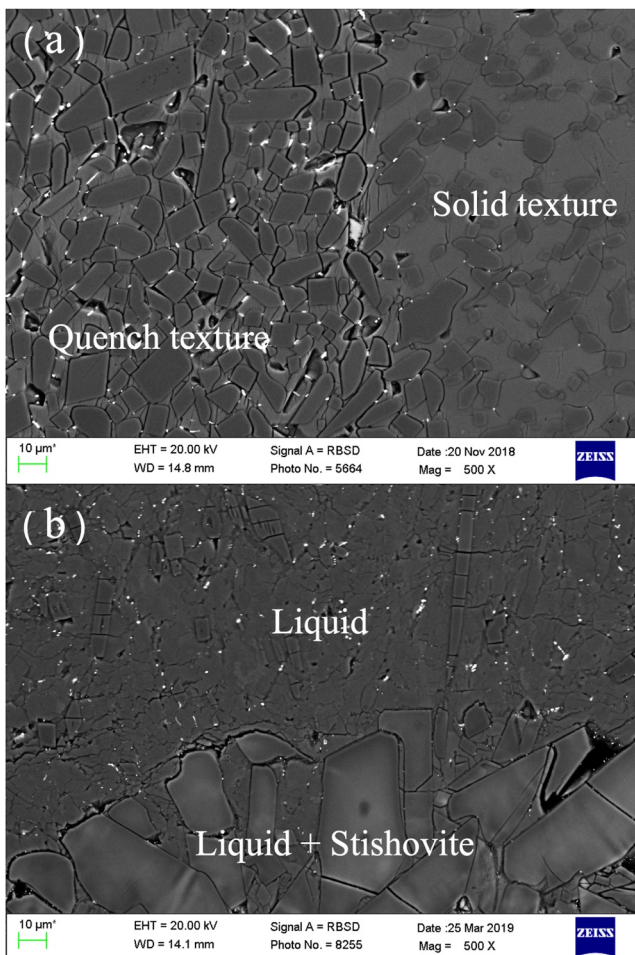

Figure 1. Scanning electron microscope images showing (a) the low degree of partial melting in the experiment for Mg$_3$Si$_7$O$_{17}$ at P = 24 GPa and T = 2750 ± 100 K, with quench texture on the left, and solid texture on the right, and (b) the experimental run product for Mg$_4$Si$_6$O$_{16}$ at P = 24 GPa and T = 2750 ± 100 K where the sample was above the solidus; large stishovite crystals (bottom) coexist with a quenched liquid phase.

3. Sample Analysis

In the experiments for Mg$_4$Si$_6$O$_{16}$ and Mg$_3$Si$_7$O$_{17}$ heated with 450 W (T = 2650 ± 100 K) (Table 1), we find a crystalline matrix with well-developed triple junctions (similar to the right side of the sample in Figure 1a), showing that they were performed at sub-solidus conditions, consistent with the prediction by de Koker et al. (2013).
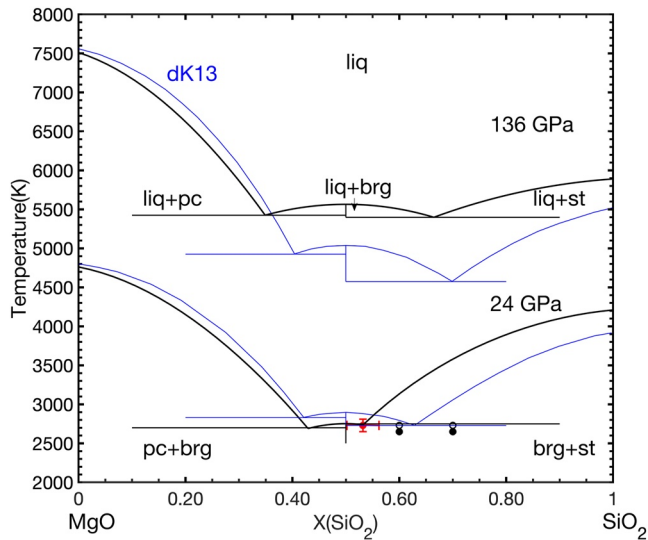
In the higher-T experiments (T = 2750 ± 100 K) for Mg$_3$Si$_7$O$_{17}$, we observe a quench texture in the recovered sample coexisting with the solid (Figure 1a). Within the quench texture we observe small bridgmanite and stishovite grains (both a few µm in size, also confirmed by X-ray diffraction), with a small amount of liquid between them, suggesting that we have just reached super-solidus T, tightly constraining T_e, with our value in excellent agreement with the prediction by de Koker et al. (2013). In addition, some of the stishovite grains appear to have grown at the expense of the liquid during quench, as indicated by the lighter-colored rims. The amount of melt preserved in the sample is too small for it to be analyzed by EPMA.

For the Mg$_4$Si$_6$O$_{16}$ sample heated with 470 W (T = 2750 ± 100 K), by contrast, we observe a liquid quench texture, coexisting with acicular stishovite crystals, some of which reach lengths of 50 µm and widths of 30 µm, indicating a liquidus assemblage (Figure 1b). The identification of stishovite as the liquidus phase for X_{SiO_2} = 0.6 starting composition suggests that the liquid evolves toward a MgSiO$_3$-rich composition. Microprobe analysis of 32 spots in the quenched melt shows values in the range of X_{SiO_2} = 0.49 – 0.60, reflecting small-scale heterogeneity (Figure 1b), with an average of X_{SiO_2} = 0.53 ± 0.03 (Figure 2) that accurately represents the bulk melt. As the melting experiment for Mg$_3$Si$_7$O$_{17}$ with virtually the same heating power suggests that we are very close to T_e, the liquid composition in the Mg$_4$Si$_6$O$_{16}$ experiment constrains the eutectic composition in the MgSiO$_3$-SiO$_2$ system.

This is a significantly lower eutectic X_{SiO_2}-value at P = 24 – 25 GPa than calculated by de Koker et al. (2013) based on ab-initio simulations with

Figure 2. MgO-SiO$_2$ melting relations computed from our thermodynamic model at 24 GPa (bottom black graph), based on the experiments performed in the MgSiO$_3$-SiO$_2$ system, combined with the result for the MgO-MgSiO$_3$ system from Liebske and Frost (2012). The eutectic composition (red circle with error) is determined based on an experiment for Mg$_4$Si$_6$O$_{16}$ at P = 24 GPa and T = 2750 $\pm$ 100 K (open circle); starting compositions and temperature of the other three experiments (Table 1) are also shown, with the filled black circles for the experiments at T = 2650 $\pm$ 100 K showing experiments that remained below the solidus. Melting relations at P = 136 GPa (top black graph) computed from our model. For comparison we include melting relations from the model of de Koker et al. (2013) (dK13, blue) both at P = 24 GPa and P = 136 GPa. Abbreviations: pc for periclase, brg for bridgmanite, st for stishovite and liq for liquid.

X_{SiO_2} = 0.63 (Figure 2) or extrapolated from DAC experiments by Ozawa et al. (2018) with X_{SiO_2} = 0.58, but consistent with X_{SiO_2} = 0.51 modeled by Belmonte et al. (2017).

4. Thermodynamic Description

4.1. Model Formulation and Parameters

We extend the previously established thermodynamic model for melting phase relations in MgO-MgSiO$_3$ from Liebske and Frost (2012) to the MgO-SiO$_2$ system by using the location of both eutectic points as constraints. For a closed formulation with a minimum number of parameters, we represent all liquids through the oxide components MgO and SiO$_2$, and use MgO periclase, MgSiO$_3$ bridgmanite and SiO$_2$ stishovite as solid phases. At both eutectics we equate the chemical potentials (μ),

$$\mu_{\text{MgSiO}_3}^{\text{solid}} = \mu_{\text{MgO}}^{\text{liquid}} + \mu_{\text{SiO}_2}^{\text{liquid}} \quad \text{and} \quad \mu_{\text{MgO}}^{\text{solid}} = \mu_{\text{MgO}}^{\text{liquid}}, \tag{1}$$

$$\mu_{\text{MgSiO}_3}^{\text{solid}} = \mu_{\text{MgO}}^{\text{liquid}} + \mu_{\text{SiO}_2}^{\text{liquid}} \quad \text{and} \quad \mu_{\text{SiO}_2}^{\text{solid}} = \mu_{\text{SiO}_2}^{\text{liquid}}, \tag{2}$$

respectively. The chemical potentials of the liquids can be expanded into a standard state potential $\mu_{\text{MgO}}^{0,\text{liquid}}$ for MgO ($\mu_{\text{SiO}_2}^{0,\text{liquid}}$ for SiO$_2$), and an activity term $a_{\text{MgO}} = X_{\text{MgO}} \gamma_{\text{MgO}}$ ($a_{\text{SiO}_2} = X_{\text{SiO}_2} \gamma_{\text{SiO}_2}$), with γ_{MgO} (γ_{SiO_2}) the activity coefficient:

$$\mu_{\text{MgO}}^{\text{solid}} = \mu_{\text{MgO}}^{0,\text{liquid}} + R \cdot T \cdot \ln\left(X_{\text{MgO}} \gamma_{\text{MgO}}\right), \tag{3}$$

$$\mu_{\text{SiO}_2}^{\text{solid}} = \mu_{\text{SiO}_2}^{0,\text{liquid}} + R \cdot T \cdot \ln\left(X_{\text{SiO}_2} \gamma_{\text{SiO}_2}\right), \tag{4}$$

$$\mu_{\text{MgSiO}_3}^{\text{solid}} = \mu_{\text{MgO}}^{0,\text{liquid}} + R \cdot T \cdot \ln\left(X_{\text{MgO}} \gamma_{\text{MgO}}\right) + \mu_{\text{SiO}_2}^{0,\text{liquid}} + R \cdot T \cdot \ln\left(X_{\text{SiO}_2} \gamma_{\text{SiO}_2}\right). \tag{5}$$

In a binary symmetric solution model, the activity coefficients are described as

$$R \cdot T \cdot \ln\left(\gamma_{\text{MgO}}\right) = W_{\text{MgO−SiO}_2} \left(1 - X_{\text{MgO}}\right)^2 \tag{6}$$

and

$$R \cdot T \cdot \ln\left(\gamma_{\text{SiO}_2}\right) = W_{\text{MgO−SiO}_2} \left(1 - X_{\text{SiO}_2}\right)^2, \tag{7}$$

where $W_{\text{MgO−SiO}_2}$ is a Margules interaction parameter. We formulate a T-dependence of $W_{\text{MgO−SiO}_2} = W_H - W_S T$, but with experiments performed only at 24 GPa, a P dependent model cannot be fit. Using a more complex solution model, for example, asymmetric as in Baron et al. (2017) and de Koker et al. (2013), does not change the width of the stability field for MgSiO$_3$ plus liquid as pointed out by de Koker et al. (2013), and with the number of data collected here, more complex models are not sufficiently constrained.

The standard state chemical potentials $\mu_{\text{MgO}}^{0,\text{liquid}}$ and $\mu_{\text{SiO}_2}^{0,\text{liquid}}$ are determined from melting of MgO and SiO$_2$, respectively. For MgO, for example,

$$\mu_{\text{MgO}}^{0,\text{liquid}} - \mu_{\text{MgO}}^{0,\text{solid}} = \overline{G}_{f,\text{MgO}} = 0 \tag{8}$$

holds, with $\overline{G}_{f,\text{MgO}}$ the Gibbs energy of fusion. Standard state chemical potentials for the liquid components ($\mu_{\text{MgO}}^{0,\text{liquid}}$ and $\mu_{\text{SiO}_2}^{0,\text{liquid}}$) are evaluated based on the thermodynamic model by de Koker et al. (2013) (*cf.* Supporting Information S1 for an extended presentation); $\mu_{\text{MgO}}^{\text{solid}}$, $\mu_{\text{MgSiO}_3}^{\text{solid}}$ and $\mu_{\text{SiO}_2}^{\text{solid}}$ are based on the Birch-Murnaghan Mie-Grüneisen model (*cf.* Supporting Information S1 for an extended presentation; e.g., Chust et al., 2017) for

MgO periclase, SiO_2 stishovite and $MgSiO_3$ bridgmanite used in de Koker et al. (2013). Both models and corresponding databases are implemented in the BurnMan thermoelastic toolbox (Cottaar et al., 2014).

Using the SiO_2 liquid and stishovite parameters in the thermodynamic model of de Koker et al. (2013), we find that an effective interaction parameter of -200 kJ/mol $\leq W_{MgO\ SiO_2} \leq -250$ kJ/mol is required to reproduce the solidus temperatures of $T \sim 2750$ K for $MgSiO_3$-SiO_2 determined here. Nevertheless, we cannot find a satisfactory solution for $W_{MgO-SiO_2}$ that describes $X_{SiO_2} = 0.53 \pm 0.03$ for the eutectic adequately. This is not surprising considering that in the model of de Koker et al. (2013) liquidus T decreases rapidly from the high melting temperature (T_m) of stishovite with increasing MgO content. We therefore consider modifications in the coefficients for the thermodynamic description of liquid SiO_2 in the model of de Koker et al. (2013) (Tables S1 and S3 in Supporting Information S1). In order to reasonably match T_m of SiO_2, we also consider changes in the thermodynamic description for stishovite which we restrict to reference energy and entropy (Table S4 in Supporting Information S1).

Rather than optimizing the thermodynamic parameters for SiO_2 liquid and stishovite separately from the Margules parameter $W_{MgO-SiO_2}$, we jointly determine them by using a least square Monte Carlo minimization. With only two constraints (the eutectics), the problem is underdetermined, and initial guesses and bounds for the parameters are important. We make choices that are guided by physical insight into (a) the thermodynamic parameters of SiO_2 liquid, (b) the melting curve of stishovite, (c) the range of values for the effective interaction parameter $W_{MgO-SiO_2}$ at 24 GPa discussed above, and (d) mixing properties for the liquids along the MgO-SiO_2 join estimated by de Koker et al. (2013). The melting point of $MgSiO_3$ at 24 GPa is not used as a constraint; rather, it serves as a consistency test for the results of the mixing model and the thermodynamic parameters for SiO_2 liquid. Using 1,000 Monte Carlo passes, we find an optimized thermodynamic description for SiO_2 (Tables S1 and S3 in Supporting Information S1) and model a T-dependent Margules parameter of

$$W_{MgO-SiO_2} = -174(\pm 4)\frac{kJ}{mol} - 17(\pm 2)\frac{J}{mol \cdot K}T. \tag{9}$$

The value for W_S is consistent with the entropy of mixing reported by de Koker et al. (2013) from ab-initio simulations. At 25 GPa, minimum values for excess Gibbs energy of mixing in the various thermodynamic models developed for high P applications fall in the range of $-(50-60)$ kJ/mol, with the exception of that of Miyazaki and Korenaga (2019) (Figure S2 in Supporting Information S1). At this (and higher) P, the mixing model by de Koker et al. (2013) shows very little asymmetry.

Any P dependence discussed below hinges on the thermodynamic description of the liquid and solid components, and an implicit P dependence of the interaction parameter via T. In this context, not only the evolution of the eutectic points with P are important, but also the melting curve $T_m - P$ for $MgSiO_3$ as a consistency check as it involves both thermodynamic parameters for SiO_2 and the parametrization of $W_{MgO-SiO_2}$ (Equation 9), similar to its role at 24 GPa.

4.2. MgO-SiO_2 Melting Relations at Experimental Pressure (24 GPa)

Combining $W_{MgO-SiO_2}$ and the modified thermodynamic parameters as described above, we compute the MgO-SiO_2 phase diagram at $P = 24$ GPa (Figure 2). It hinges on five points: T_m of MgO, $MgSiO_3$, and SiO_2 and the two eutectics.

$T_m = 4760$ K for MgO computed by BurnMan at 24 GPa is very close to that reported in de Koker et al. (2013) (4800 K) (Figures 2 and 3a), and agrees with DAC experiments by Du and Lee (2014) and Kimura et al. (2017) in the same P range. Ab-initio results by Alfè (2005) and Soubiran and Militzer (2020) report T_m higher and smaller by ~ 250 K, respectively.

For stishovite, we compute $T_m = 4210 \pm 120$ K at 24 GPa, with the uncertainty (two standard deviations) determined by 1,000 Monte Carlo passes, varying the thermodynamic parameters (Tables S1–S4 in Supporting Information S1), slightly higher than $T_m = 3920$ K from de Koker et al. (2013), but consistent with DAC experiments that bracket melting with $T = 3800 - 4300$ K at $P = 22 - 29$ GPa (Shen & Lazor, 1995) and $T = 4000 - 4400$ K at $P = 27 - 29$ GPa (Andrault et al., 2020; Figures 2 and 3b).
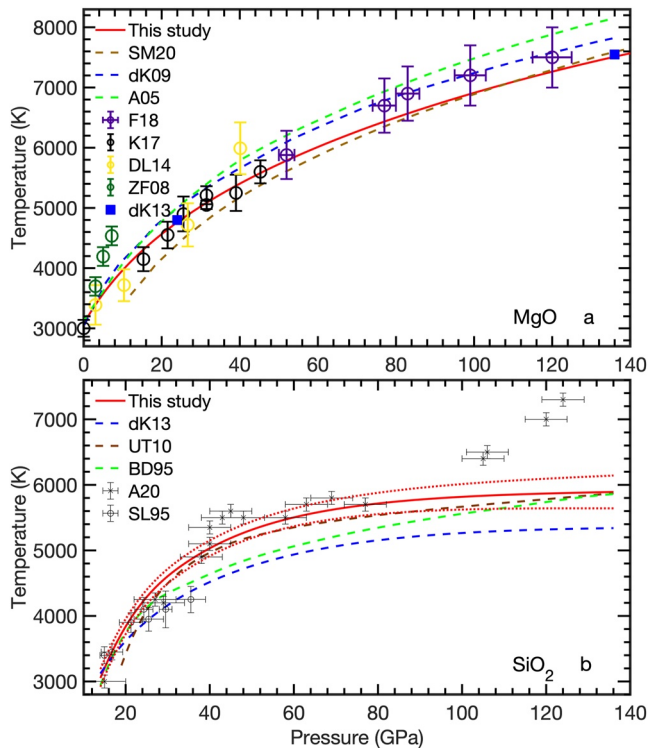
Figure 3. Melting curves of MgO (panel a) SiO$_2$ stishovite (panel b). For MgO, we use the melting curve from the BurnMan package, based on the model of de Koker et al. (2013) (red). We show data from multi-anvil (Zhang & Fei, 2008; ZF08, dark green) and diamond anvil cell experiments by Du and Lee (2014) (DL14, yellow), Kimura et al. (2017) (K17, black) and Fu et al. (2018) (F18, purple), and ab-initio melting curves (dashed lines) from Alfè (2005) (A05, green) and Soubiran and Militzer (2020) (SM20, brown). The model of de Koker and Stixrude (2009) (dK09, blue) matches ab initio properties of the liquid with a thermodynamic assessment of the solid by Stixrude and Lithgow-Bertelloni (2005). For stishovite, results from our thermodynamic model are shown by the red solid line, the red dotted lines represent uncertainties calculated by Monte Carlo simulations (two standard deviations). We include data from diamond anvil cell experiments by Shen and Lazor (1995) (SL95, crosses) and Andrault et al. (2020) (A20, circles). Previously determined melting curves (dashed lines) from ab-initio simulations by Usui and Tsuchiya (2010) (UT10, brown) and Belonoshko and Dubrovinsky (1995) (BD95, green) and by the thermodynamic model of de Koker et al. (2013) (dK13, blue) are shown for comparison.

In our modified model, bridgmanite melts at 2750 ± 120 K at 24 GPa (Figures 2 and 4a), slightly below T_m = 2800 – 2900 K bracketed in MA experiments by Ito and Katsura (1992), DAC experiments by Zerr and Boehler (1993), the thermodynamic assessment of Liebske and Frost (2012) (2820 K), and molecular dynamics results by Di Paola and Brodholt (2016) in the same P range. T_m from the thermodynamic assessments of de Koker et al. (2013) falls slightly above our error bar estimated in the Monte Carlo simulations, the experiments by Shen and Lazor (1995) report a significantly higher value. The relatively low T_m of bridgmanite at 24 GPa in our model is directly linked to its narrow stability range on the liquidus in terms of X_{SiO_2}, especially for the SiO$_2$-rich side of the phase diagram. Enhancing bridgmanite stability, for example, by a constant shift of the reference energy in the underlying thermodynamic model of the solid, would inevitably move the eutectic point(s) further away from MgSiO$_3$, making it impossible to reproduce the experimental results.

The eutectic points at 24 GPa themselves are reproduced well in the Monte Carlo simulations with T_e = 2690 ± 100 K at X_{SiO_2} = 0.43 ± 0.01 and T_e = 2740 ± 120 K at X_{SiO_2} = 0.53 ± 0.01. The eutectic T of the latter is smaller than T_m for MgSiO$_3$ by 10 K only, reflecting the flat liquidus curve in the vicinity of MgSiO$_3$ (Figure 2). Similar to X_{SiO_2}, a slightly smaller value of T_e for the MgO-MgSiO$_3$ eutectic is consistent with the thermodynamic assessment of Belmonte et al. (2017) at uppermost LM pressure.

### 4.3. MgO-SiO$_2$ Melting Relations at Lower Mantle Pressure

As mentioned above, the melting curves for MgO and SiO$_2$ provide important anchor points for the phase relations (Equation 8) at higher P, and that of MgSiO$_3$ serves as a test for the validity and consistency of the liquid model.

For MgO, our melting curve matches DAC data (Du & Lee, 2014; Fu et al., 2018; Kimura et al., 2017) for P throughout the lower mantle within their margins of error (Figure 3a), reaching T_m = 7510 K at P = 136 GPa, CMB pressure, similar to de Koker et al. (2013) and ab-initio simulations by Soubiran and Militzer (2020) using thermodynamic integration. Previous assessments by de Koker and Stixrude (2009) and direct two-phase ab-initio simulations by Alfè (2005) show higher T_m, but still within experimental uncertainty.

With the changes in the thermodynamic parameters for SiO$_2$ liquid and stishovite, T_m of SiO$_2$ at P = 24 GPa is larger by ∼ 300 K compared to de Koker et al. (2013), a difference that increases to ∼ 550 K at CMB pressure (Figures 2 and 3b). However, our computed melting curve closely follows the experimental data on T_m by Andrault et al. (2020) up to 80 GPa; for P > 30 GPa our melting curve is within the margin of error of that computed by Usui and Tsuchiya (2010), and they approach the same value at CMB pressures. As has been pointed out by de Koker et al. (2013), the potential presence of CaCl$_2$-structured SiO$_2$ (Tsuchida & Yagi, 1989) is expected to have a small effect on T_m. However, the reconstructive phase transition of SiO$_2$ to seifertite in the lowermost mantle (Das et al., 2020; Dubrovinsky et al., 2001) will expand the stability range of solid SiO$_2$ to higher T, an effect that can inherently not be captured by our model, and may account for the divergence of our model with the data by Andrault et al. (2020) for P >100 GPa.

For MgSiO$_3$, the melting curve predicted by our model shows a steep initial increase with P (Figure 4), closely following the trend of the DAC experiments (Shen & Lazor, 1995; Zerr & Boehler, 1993) to 40 GPa, and, with larger scatter in the data, to 62 GPa, the highest P achieved in Zerr and Boehler (1993), and that of the shock wave experiments by Fei et al. (2021) for much of the lower mantle P-range (50–80 GPa). However, shock wave experiments (Fei et al., 2021; Fratanduono et al., 2018; Mosenfelder et al., 2009) vary largely in their estimates of the
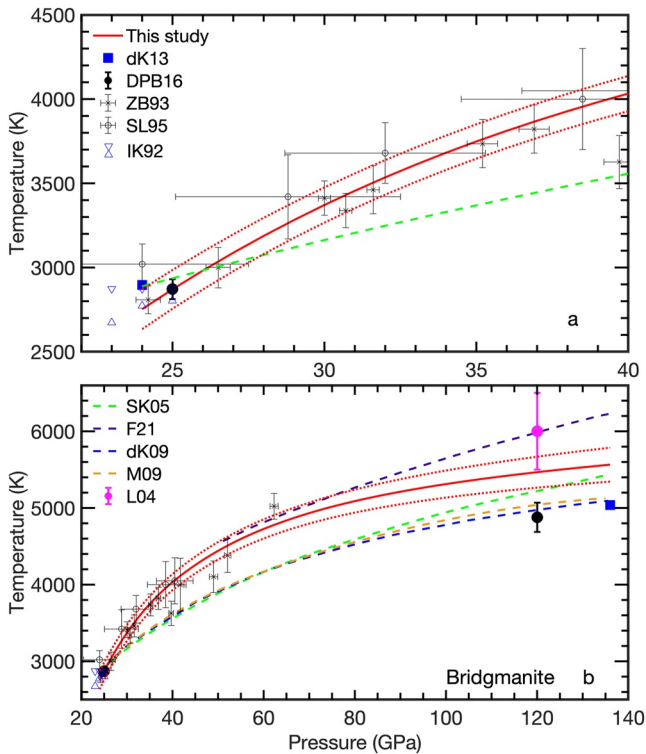
Figure 4. Melting curves for $MgSiO_3$ bridgmanite at lower mantle pressures ($20-40$ GPa at the top and $20-140$ GPa at the bottom). Results from our thermodynamic model are shown byd solid lines, the red dotted lines represent uncertainties calculated by Monte Carlo simulations. Multi-anvil experiments (Ito & Katsura, 1992; IK92, blue triangles up and down) bracket melting, and melting temperatures in diamond anvil cell experiments are reported by Zerr and Boehler (1993) (ZB93, crosses) and Shen and Lazor (1995) (SL95, open circles), and a shock melting point by Luo et al. (2004) (L04, magenta). Melting temperatures from ab-initio simulations by Di Paola and Brodholt (2016) (DPB16, filled black circles) and the model of de Koker et al., 2013 (dK13, blue squares) as well as melting curves (dashed lines) determined based on shock wave experiments by Fei et al. (2021) (F21, purple) and Mosenfelder et al. (2009) (M09, orange) from ab-initio simulations by Stixrude and Karki (2005) (SK05, green), and the model by de Koker and Stixrude (2009) (dK09, blue) are included.

melting curve. At higher P, our predicted $T_m - P$ curve flattens and reaches 5560 ± 220 K at 136 GPa. The melting temperature predicted by Stixrude and Karki (2005) at CMB P is within the margin of error of our model, but their melting curve shows a more uniform increase for LM pressure.

The consistency of predicted melting curve evolution with prior data for all three congruently melting compositions along the MgO-SiO_2 join allows us to calculate the phase diagram at $P = 136$ GPa with some confidence (Figure 2) and to explore the evolution of both eutectics in terms of X_{SiO_2} (Figure 5) and T_e (Figure 6).

In agreement with previous work, we find that both eutectics move away from $MgSiO_3$ with increasing P. For the MgO-$MgSiO_3$ eutectic, X_{SiO_2} shifts to lower values with P significantly faster than in the models of de Koker et al. (2013) and Liebske and Frost (2012) or the experimental brackets determined in the DAC by Ohnishi et al. (2017) between 45 and 70 GPa. The P dependence of the eutectic composition for MgO-$MgSiO_3$ agrees well with a second set of DAC experiments by Ozawa et al. (2018) over the P range of the entire LM. The MgO-$MgSiO_3$ eutectic in our model has a minimum value of $X_{SiO_2} = 0.32 \pm 0.02$ at $P \sim 60$ GPa, beyond which it increases quasi-linearly with P to reach $X_{SiO_2} = 0.35 \pm 0.02$ at CMB pressure. This behavior stems from the different P evolution of the melting curves for MgO (Figure 3a) and $MgSiO_3$ (Figure 4b): At P of the uppermost LM, the melting curve of $MgSiO_3$ is steeper than the one of MgO, leading to a rapid decrease in eutectic X_{SiO_2}. At $P > 60$ GPa, the $T_m - P$ slope for $MgSiO_3$ is flatter than the one for MgO, shifting eutectic X_{SiO_2} to larger values.

As discussed above, the $MgSiO_3$-SiO_2 eutectic composition is close to $MgSiO_3$ with $X_{SiO_2} = 0.53 \pm 0.01$ at $P = 24$ GPa in our model, consistent with Belmonte et al. (2017), but significantly lower than X_{SiO_2} calculated by de Koker et al. (2013). As T_m for SiO_2 does not increase with P at the same rate as that for $MgSiO_3$, eutectic X_{SiO_2} moves to larger values with P uniformly, reaching a value of $X_{SiO_2} = 0.66 \pm 0.01$ at 136 GPa. Experiments by Ozawa et al. (2018) at $P = 128$ GPa and $P = 139$ GPa agree well with our prediction, as for the MgO-$MgSiO_3$ eutectic, with values that are smaller than the model of de Koker et al. (2013). While Baron et al. (2017) assumed the chemical evolution of the eutectic following de Koker et al. (2013) in their data analysis, the actual composition reported for one sample at $P = 48$ GPa reveals a significantly lower value with $X_{SiO_2} = 0.59$, within the margin of error of our model prediction, and in general agreement with data by Ozawa et al. (2018) at $P = 41$ GPa. With a higher T_m for lowermost mantle P due to the presence of seifertite, X_{SiO_2} would move to slightly smaller values.

Eutectic temperatures in the MgO-$MgSiO_3$ and $MgSiO_3$-SiO_2 systems are very close to one another, rising from $T_e = 2690 \pm 100$ K and $T_e = 2740 \pm 120$ K at $P = 24$ GPa to $T_e = 5420 \pm 180$ K and $T_e = 5390 \pm 230$ K at $P = 136$ GPa, respectively (Figures 2 and 6). The MgO-$MgSiO_3$ and $MgSiO_3$-SiO_2 eutectic temperatures cross at $P \sim 125$ GPa, reflecting the opposing trends of eutectic X_{SiO_2} (Figure 5). The difference between T_e and the melting curve of $MgSiO_3$ does not exceed 200 K in the entire LM. At CMB pressure, our model shows higher T_e by 500–700 K than the models of de Koker et al. (2013) and Liebske and Frost (2012) for MgO-$MgSiO_3$, and higher T_e by 800 K compared to de Koker et al. (2013) for $MgSiO_3$-SiO_2. The eutectic T estimated by Baron et al. (2017) appear rather low in this context.
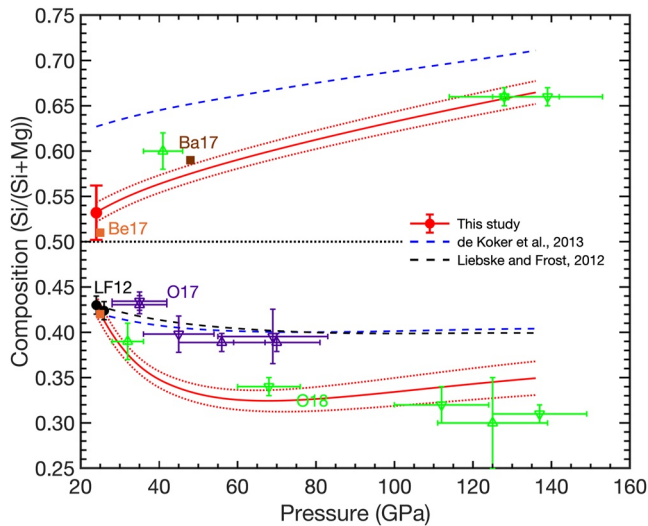
Figure 5. Eutectic compositions in the MgO-SiO$_2$ system at lower mantle pressures. Filled circles indicate eutectic liquid compositions based on our multi-anvil press experiments (red) and those by Liebske and Frost (2012) (LF12, black). Diamond anvil cell experiments by Baron et al. (2017) (Ba17, brown), Ozawa et al. (2018) (O18, green) and Ohnishi et al. (2017) (O17, purple) are included, with triangles in the latter two bracketing the eutectic composition, along with results by Belmonte et al. (2017) (Be17, orange) at $P = 25$ GPa. Results from our model are shown by the red solid curves with uncertainties from Monte Carlo simulations given by red dotted curves; they are compared to previous models by Liebske and Frost (2012) (black dashed curve) and de Koker et al. (2013) (blue dashed curves).

5. Melting Near the Core-Mantle Boundary

This similarity in T_e, and therefore the solidus T, for MgO-MgSiO$_3$ and MgSiO$_3$-SiO$_2$ predicted here suggests that melting of basalt at lower T than peridotite (Andrault et al., 2014; Kuwahara et al., 2018; Pradhan et al., 2015; Tateno et al., 2014, 2018), invoked as an explanation for the occurrence of the ULVZ in the lowermost mantle (e.g., Thorne et al., 2019), is not simply tied to its higher X_{SiO_2} value. Rather, further differences in chemical composition will influence T_m and melt relations either directly within a solid solution (e.g., a higher FeO or Al$_2$O$_3$ content in bridgmanite) or through changes in the resulting phase assemblage. Compared to mantle peridotite (Workman & Hart, 2005), oceanic crust is strongly enriched in Al$_2$O$_3$, CaO, and Na$_2$O, while the FeO content is similar in both lithologies (e.g., Chemia et al., 2015). For oceanic crust this leads to a phase assemblage that differs in various aspects from peridotite at LM pressure: (a) it contains significantly more CaSiO$_3$ perovskite (e.g., Chust et al., 2017) and (b) SiO$_2$ occurs as a free phase rather than the ferropericlase solid solution. Both CaSiO$_3$ perovskite and SiO$_2$ stishovite dissolve a few % of Al$_2$O$_3$ and very little FeO (e.g., Kuwahara et al., 2018; Tateno et al., 2018), while ferropericlase in a peridotitic composition contains up to 20% FeO (e.g., Chust et al., 2017; Kuwahara et al., 2018). Further, (c) for basalt an Al$_2$O$_3$ dominated mineral occurs in the LM, either as Ca-ferrite (Irifune & Ringwood, 1993; Tateno et al., 2018) or the NAL phase (Imada et al., 2012; Kato et al., 2013). As a consequence of these phase relations, bridgmanite in a basaltic composition can be expected to be significantly enriched in FeO compared to a mantle peridotite. A high FeO content in partial melts from basalt compositions at LM pressure (Kuwahara et al., 2018; Pradhan et al., 2015; Tateno et al., 2018) suggests that the solidus T in the resulting bridgmanite is significantly lower tha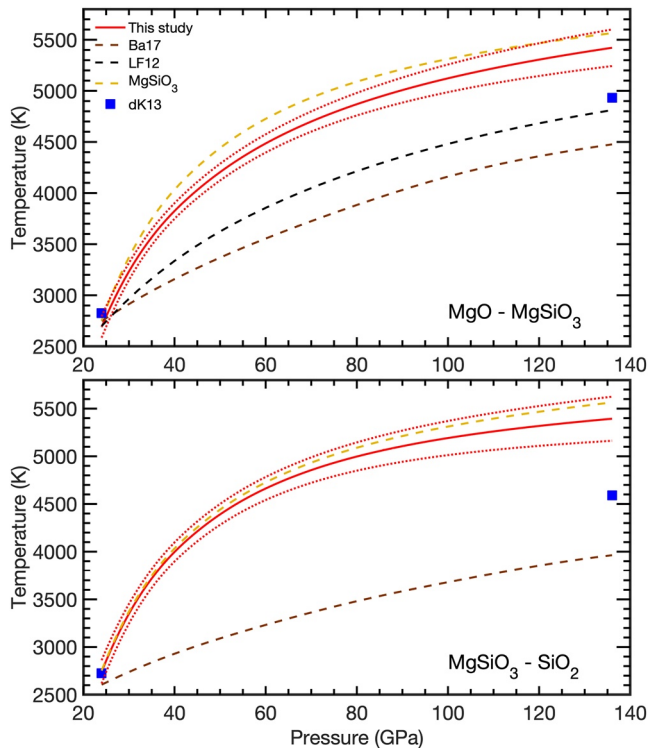n for the eutectic in the MgSiO$_3$-SiO$_2$ system established here. This is further supported by the observation that while CaSiO$_3$ perovskite is the phase on the solidus in peridotite at LM pressure, it becomes the liquidus phase for MORB compositions, and bridgmanite simultaneously becomes the solidus phase (Kuwahara et al., 2018; Pradhan et al., 2015; Tateno et al., 2014, 2018).

However, the chemical complexity of natural or model systems investigated in these studies makes it challenging to disentangle the causes for these discrepancies. In order to analyze the influence of other chemical components in a systematic way by building up a thermodynamic model for mantle compositions, controlled melting experiments in the MA press like the ones performed here are required, ideally for MgO/SiO$_2$ ratios of the eutectic compositions. Not only dictated by chemical abundances, but also the crystal-chemical and phase relation arguments outlined in the previous paragraph, such a model should be built from the two-component system explored here to the FeO-MgO-SiO$_2$ and subsequently the FeO-MgO-Al$_2$O$_3$-SiO$_2$ systems. These will provide successive insights into the melting relations, for example, from the influence of FeO (and Al$_2$O$_3$) in the bridgmanite solid solution and from an additional Al$_2$O$_3$-rich phase in the assemblage.

With bridgmanite the liquidus phase in a peridotite composition (Tateno et al., 2014), the shallow slope of its melting curve through much of the LM opens the possibility that crystallization of the mantle may have indeed initiated from the middle of the mantle, as proposed in a number of studies (Andrault, 2019; Stixrude et al., 2009). Most prominently, this would lead to the formation of a basal magma ocean (Herzberg et al., 2013; Labrosse et al., 2007), and a separation of two magma ocean reservoirs would strongly be aided if the crystallizing layer is neutrally buoyant. While bridgmanite is denser than the coexisting liquid with $X_{SiO_2} < 0.5$, the strong partitioning of FeO into the melt (Nomura et al., 2011; Tateno et al., 2014) may lead to a situation in which the density contrast between magma ocean liquid and crystallizing bridgmanite is minimal.

With the eutectic in the MgSiO$_3$-SiO$_2$ system exceeding $X_{SiO_2} = 0.60$ at $P \sim 70$ GPa, magma oceans in rocky exoplanets would likely crystallize bridgmanite rather than stishovite for most plausible scenarios, and therefore

Figure 6. Eutectic temperatures in the MgO-MgSiO$_3$ (top) and the MgSiO$_3$-SiO$_2$ systems (bottom) at lower mantle pressures. Our results are shown by red curves (uncertainties in dotted lines from Monte Carlo simulations), those of Baron et al. (2017) in brown (Ba17), by de Koker et al. (2013) at $P = 24$ GPa and at $P = 136$ GPa by blue symbols (dK13). For MgO-MgSiO$_3$, eutectic temperatures of the model by Liebske and Frost (2012) are shown in black (LF12). For reference, we include the MgSiO$_3$ melting curve from our model (golden dashed curves) in both panels.

not create a very dense SiO$_2$-dominated layer deep in their mantle that would impede the onset of convection and therefore efficient heat loss from the planet (e.g., Tosi et al., 2013).

6. Conclusions

In multi-anvil experiments at 24 GPa we have measured the compositions of partial melts formed from a Mg$_4$Si$_6$O$_{16}$ starting composition at a temperature of 2750 ± 100 K. Electron microscope and microprobe analysis of the recovered experimental charges reveals that stishovite is the crystalline phase at the liquidus, and the coexisting liquid has a composition of $X_{SiO_2} = 0.53 \pm 0.03$. This implies an MgSiO$_3$-SiO$_2$ eutectic that is very close to MgSiO$_3$ bridgmanite in composition which is therefore the liquidus phase in the MgO-SiO$_2$ system over a compositional range from $X_{SiO_2} = 0.43$ (Liebske & Frost, 2012) to $X_{SiO_2} = 0.53$, with very similar eutectic (solidus) temperatures. Combining our eutectic with that of Liebske and Frost (2012) for MgO-MgSiO$_3$ and thermodynamic models for the liquid components SiO$_2$ and MgO as well as the solid phases SiO$_2$ stishovite, MgO periclase and MgSiO$_3$ bridgmanite, we have modeled the melting phase relations in the MgO-SiO$_2$ system using a symmetric solution model for the liquid components.

The extrapolation of our thermodynamic description for melting relations to higher pressures hinges on its temperature dependence and the melting curves of MgO and SiO$_2$. Our model describes the melting curve of MgSiO$_3$ bridgmanite consistent with diamond anvil cell experiments up to 60 GPa, and recent shock wave experiment to 80 GPa. In our model, the eutectic compositions move to $X_{SiO_2} = 0.35 \pm 0.02$ and $X_{SiO_2} = 0.66 \pm 0.02$ at core-mantle boundary pressure, respectively. Eutectic temperatures of these two compositions remain similar, suggesting that lower solidus temperatures of basalt over peridotite in the deep mantle, which has been observed in a series of prior experiments on natural or model compositions, must be related to chemical components other than SiO$_2$ and MgO.

Data Availability Statement

In compliance with AGU's data availability requirements, the microprobe analysis of the melt in the experiment S7238 (Table 1) at the basis of the current work is available on Figshare (https://doi.org/10.6084/m9.figshare.16837090.v1).

References

Alfè, D. (2005). Melting curve of MgO from first-principles simulations. *Physical Review Letters*, *94*, 235701. https://doi.org/10.1103/physrevlett.94.235701

Andrault, D. (2019). Thermodynamical constraints on the crystallization of a deep magma-ocean on Earth. *Comptes Rendus Geoscience*, *351*, 221–228. https://doi.org/10.1016/j.crte.2018.06.003

Andrault, D., Morard, G., Garbarino, G., Mezouar, M., Bouhifd, M. A., & Kawamoto, T. (2020). Melting behavior of SiO$_2$ up to 120 GPa. *Physics and Chemistry of Minerals*, *47*, 10. https://doi.org/10.1007/s00269-019-01077-3

Andrault, D., Pesce, G., Bouhifd, M. A., Bolfan-Casanova, N., Hénot, J. M., & Mezouar, M. (2014). Melting of subducted basalt at the core-mantle boundary. *Science*, *344*, 892–895. https://doi.org/10.1126/science.1250466

Baron, M. A., Lord, O. T., Myhill, R., Thomson, A. R., Wang, W., Trønnes, R. G., & Walter, M. J. (2017). Experimental constraints on melting temperatures in the MgO-SiO$_2$ system at lower mantle pressures. *Earth and Planetary Science Letters*, *472*, 186–196. https://doi.org/10.1016/j.epsl.2017.05.020

Belmonte, D., Ottonello, G., Zuccolini, M. V., & Attene, M. (2017). The system MgO-Al$_2$O$_3$-SiO$_2$ under pressure: A computational study of melting relations and phase diagrams. *Chemical Geology*, *461*, 54–64. https://doi.org/10.1016/j.chemgeo.2016.11.011

Belonoshko, A. B., & Dubrovinsky, L. S. (1995). Molecular dynamics of stishovite melting. *Geochimica et Cosmochimica Acta*, *59*, 1883–1889. https://doi.org/10.1016/0016-7037(95)00071-7

Boukaré, C. E., Ricard, Y., & Fiquet, G. (2015). Thermodynamics of the MgO-FeO-SiO$_2$ system up to 140 GPa: Application to the crystallization of Earth's magma ocean. *Journal of Geophysical Research: Solid Earth*, *120*, 6085–6101. https://doi.org/10.1002/2015jb011929

Chemia, Z., Dolejš, D., & Steinle-Ne umann, G. (2015). Thermal effects of variable material properties and metamorphic reactions in a three-component subducting slab. *Journal of Geophysical Research: Solid Earth*, *120*, 6823–6845. https://doi.org/10.1002/2015jb012080

Chust, T. C., Steinle-Neumann, G., Dolejš, D., Schuberth, B. S. A., & Bunge, H. P. (2017). MMA-EoS: A computational framework for mineralogical thermodynamics. *Journal of Geophysical Research: Solid Earth*, *122*, 9881–9920. https://doi.org/10.1002/2017jb014501

Cottaar, S., Heister, T., Rose, I., & Unterborn, C. (2014). BurnMan: A lower mantle mineral physics toolkit. *Geochemistry, Geophysics, Geosystems*, *15*, 1164–1179. https://doi.org/10.1002/2013gc005122

Das, P. K., Mohn, C. E., Brodholt, J. P., & Trønnes, R. (2020). High-pressure silica phase transitions: Implications for deep mantle dynamics and silica crystallization in the protocore. *American Mineralogist*, *105*, 1014–1020. https://doi.org/10.2138/am-2020-7299

Dasgupta, R. (2018). Volatile-bearing partial melts beneath oceans and continents–Where, how much, and of what compositions? *American Journal of Science*, *318*, 141–165. https://doi.org/10.2475/01.2018.06

Dauphas, N., Poitrasson, F., Burkhardt, C., Kobayashi, H., & Kurosawa, K. (2015). Planetary and meteoritic Mg/Si and δ^{30}Si variations inherited from solar nebula chemistry. *Earth and Planetary Science Letters*, *427*, 236–248. https://doi.org/10.1016/j.epsl.2015.07.008

de Koker, N., Karki, B. B., & Stixrude, L. (2013). Thermodynamics of the MgO-SiO$_2$ liquid system in Earth's lowermost mantle from first principles. *Earth and Planetary Science Letters*, *361*, 58–63. https://doi.org/10.1016/j.epsl.2012.11.026

de Koker, N., & Stixrude, L. (2009). Self-consistent thermodynamic description of silicate liquids, with application to shock melting of MgO periclase and MgSiO$_3$ perovskite. *Geophysical Journal International*, *178*, 162–179. https://doi.org/10.1111/j.1365-246x.2009.04142.x

Di Paola, C., & Brodholt, J. P. (2016). Modeling the melting of multicomponent systems: The case of MgSiO$_3$ perovskite under lower mantle conditions. *Scientific Reports*, *6*, 29830. https://doi.org/10.1038/srep29830

Du, Z., & Lee, K. K. M. (2014). High-pressure melting of MgO from (Mg, Fe) O solid solutions. *Geophysical Research Letters*, *41*, 8061–8066. https://doi.org/10.1002/2014gl061954

Dubrovinsky, L. S., Dubrovinskaia, N. A., Saxena, S. K., Tutti, F., Rekhi, S., Le Bihan, T., et al. (2001). Pressure-induced transformations of cristobalite. *Chemical Physics Letters*, *333*, 264–270. https://doi.org/10.1016/s0009-2614(00)01147-7

Elardo, S. M., Draper, D. S., & Shearer, C. K., Jr. (2011). Lunar Magma Ocean crystallization revisited: Bulk composition, early cumulate mineralogy, and the source regions of the highlands Mg-suite. *Geochimica et Cosmochimica Acta*, *75*, 3024–3045. https://doi.org/10.1016/j.gca.2011.02.033

Elkins-Tanton, L. T., Parmentier, E. M., & Hess, P. C. (2003). Magma ocean fractional crystallization and cumulate overturn in terrestrial planets: Implications for Mars. *Meteoritics & Planetary Science*, *38*, 1753–1771. https://doi.org/10.1111/j.1945-5100.2003.tb00013.x

Fei, Y., Seagle, C. T., Townsend, J. P., McCoy, C. A., Boujibar, A., Driscoll, P., et al. (2021). Melting and density of MgSiO$_3$ determined by shock compression of bridgmanite to 1254 GPa. *Nature Communications*, *12*, 876. https://doi.org/10.1038/s41467-021-21170-y

Fiquet, G., Auzende, A. L., Siebert, J., Corgne, A., Bureau, H., Ozawa, H., & Garbarino, G. (2010). Melting of peridotite to 140 gigapascals. *Science*, *329*, 1516–1518. https://doi.org/10.1126/science.1192448

Fratanduono, D. E., Millot, M., Kraus, R. G., Spaulding, D. K., Collins, G. W., Celliers, P. M., & Eggert, J. H. (2018). Thermodynamic properties of MgSiO$_3$ at super-Earth mantle conditions. *Physical Review B*, *97*, 214105. https://doi.org/10.1103/physrevb.97.214105

Fu, S., Yang, J., Zhang, Y., Liu, J., Greenberg, E., Prakapenka, V. B., et al. (2018). Melting behavior of the lower-mantle ferropericlase across the spin crossover: Implication for the ultra-low velocity zones at the lowermost mantle. *Earth and Planetary Science Letters*, *503*, 1–9. https://doi.org/10.1016/j.epsl.2018.09.014

Hernlund, J. W., & Jellinek, A. M. (2010). Dynamics and structure of a stirred partially molten ultralow-velocity zone. *Earth and Planetary Science Letters*, *296*, 1–8. https://doi.org/10.1016/j.epsl.2010.04.027

Herzberg, C., Asimow, P. D., Ionov, D. A., Vidito, C., Jackson, M. G., & Geist, D. (2013). Nickel and helium evidence for melt above the core-mantle boundary. *Nature*, *493*, 393–397. https://doi.org/10.1038/nature11771

Hinkel, N. R., & Unterborn, C. T. (2018). The star-planet connection. I. Using stellar composition to observationally constrain planetary mineralogy for the 10 closest stars. *The Astrophysical Journal*. https://doi.org/10.3847/1538-4357/aaa5b4

Hirose, K., Fei, Y., Ma, Y., & Mao, H. K. (1999). The fate of subducted basaltic crust in the Earth's lower mantle. *Nature*, *397*, 53–56. https://doi.org/10.1038/16225

Imada, S., Hirose, K., Komabayashi, T., Suzuki, T., & Ohishi, Y. (2012). Compression of Na$_{0.4}$Mg$_{0.6}$Al$_{1.6}$Si$_{0.4}$O$_4$ NAL and Ca-ferrite-type phases. *Physics and Chemistry of Minerals*, *39*, 535–530. https://doi.org/10.1007/s00269-012-0508-x

Irifune, T., & Ringwood, A. E. (1993). Phase transformations in subducted oceanic crust and buoyancy relationships at depths of 600–800 km in the mantle. *Earth and Planetary Science Letters*, *117*, 101–110. https://doi.org/10.1016/0012-821x(93)90120-x

Ito, E., & Katsura, T. (1992). *High-pressure Research: Applications to Earth and planetary Sciences. Terrapub*. (pp. 315–322). American Geophysical Union.

Johnson, E. R., Wallace, P. J., Cashman, K. V., Granados, H. D., & Kent, A. J. (2008). Magmatic volatile contents and degassing-induced crystallization at Volcán Jorullo, Mexico: Implications for melt evolution and the plumbing systems of monogenetic volcanoes. *Earth and Planetary Science Letters*, *269*, 478–487. https://doi.org/10.1016/j.epsl.2008.03.004

Kato, C., Hirose, K., Komabayashi, T., Ozawa, H., & Ohishi, Y. (2013). NAL phase in K-rich portions of the lower mantle. *Geophysical Research Letters*, *40*, 5085–5088. https://doi.org/10.1002/grl.50966

Kelemen, P. B., Shimizu, N., & Salters, V. J. (1995). Extraction of mid-ocean-ridge basalt from the upwelling mantle by focused flow of melt in dunite channels. *Nature*, *375*, 747–753. https://doi.org/10.1038/375747a0

Keppler, H., & Frost, D. J. (2005). Introduction to minerals under extreme conditions. In R. Miletich (Ed.), *Mineral behavior at Extreme conditions* (pp. 1–30). European Mineralogical Union.

Kimura, T., Ohfuji, H., Nishi, M., & Irifune, T. (2017). Melting temperatures of MgO under high pressure by micro-texture analysis. *Nature Communications*, *8*, 15735. https://doi.org/10.1038/ncomms15735

Kuwahara, H., Nomura, R., Nakada, R., & Irifune, T. (2018). Simultaneous determination of melting phase relations of mantle peridotite and mid-ocean ridge basalt at the uppermost lower mantle conditions. *Physics of the Earth and Planetary Interiors*, *284*, 36–50. https://doi.org/10.1016/j.pepi.2018.08.012

Labrosse, S., Hernlund, J. W., & Coltice, N. (2007). A crystallizing dense magma ocean at the base of the Earth's mantle. *Nature*, *450*, 866–869. https://doi.org/10.1038/nature06355

Liebske, C., & Frost, D. J. (2012). Melting phase relations in the MgO-MgSiO$_3$ system between 16 and 26 GPa: Implications for melting in Earth's deep interior. *Earth and Planetary Science Letters*, *345*, 159–170. https://doi.org/10.1016/j.epsl.2012.06.038

Luo, S. N., Akins, J. A., Ahrens, T. J., & Asimow, P. D. (2004). Shock-compressed MgSiO$_3$ glass, enstatite, olivine, and quartz: Optical emission, temperatures, and melting. *Journal of Geophysical Research*, *109*, B05205. https://doi.org/10.1029/2003jb002860

Miyazaki, Y., & Korenaga, J. (2019). On the timescale of magma ocean solidification and its chemical consequences: 1. Thermodynamic database for liquid at high pressures. *Journal of Geophysical Research: Solid Earth*, *124*, 3382–3398. https://doi.org/10.1029/2018jb016932

Monteux, J., Andrault, D., & Samuel, H. (2016). On the cooling of a deep terrestrial magma ocean. *Earth and Planetary Science Letters*, *448*, 140–149. https://doi.org/10.1016/j.epsl.2016.05.010

Mosenfelder, J. L., Asimow, P. D., Frost, D. J., Rubie, D. C., & Ahrens, T. J. (2009). The MgSiO$_3$ system at high pressure: Thermodynamic properties of perovskite, postperovskite, and melt from global inversion of shock and static compression data. *Journal of Geophysical Research*, *114*, B01203. https://doi.org/10.1029/2008jb005900

Nishihara, Y., Doi, S., Kakizawa, S., Higo, Y., & Tange, Y. (2020). Effect of pressure on temperature measurements using WRe thermocouple and its geophysical impact. *Physics of the Earth and Planetary Interiors*, *298*, 106348. https://doi.org/10.1016/j.pepi.2019.106348

Nomura, R., Hirose, K., Uesugi, K., Ohishi, Y., Tsuchiyama, A., Miyake, A., & Ueno, Y. (2014). Low core-mantle boundary temperature inferred from the solidus of pyrolite. *Science*, *343*, 522–525. https://doi.org/10.1126/science.1248186

Nomura, R., Ozawa, H., Tateno, S., Hirose, K., Hernlund, J., Muto, S., et al. (2011). Spin crossover and iron-rich silicate melt in the Earth's deep mantle. *Nature*, *473*, 199–202. https://doi.org/10.1038/nature09940

Ohnishi, S., Kuwayama, Y., & Inoue, T. (2017). Melting relations in the MgO-MgSiO$_3$ system up to 70 GPa. *Physics and Chemistry of Minerals*, *44*, 445–453. https://doi.org/10.1007/s00269-017-0871-8

Ozawa, K., Anzai, M., Hirose, K., Sinmyo, R., & Tateno, S. (2018). Experimental determination of eutectic liquid compositions in the MgO-SiO$_2$ system to the lowermost mantle pressures. *Geophysical Research Letters*, *45*, 9552–9558. https://doi.org/10.1029/2018gl079313

Palme, H., & O'Neill, H. S. C. (2003). Cosmochemical estimates of mantle composition. *Treatise on Geochemistry*, *2*, 1–38.

Pradhan, G. K., Fiquet, G., Siebert, J., Auzende, A. L., Morard, G., Antonangeli, D., & Garbarino, G. (2015). Melting of MORB at core-mantle boundary. *Earth and Planetary Science Letters*, *431*, 247–255. https://doi.org/10.1016/j.epsl.2015.09.034

Revenaugh, J., & Sipkin, S. A. (1994). Seismic evidence for silicate meting atop the 410-km mantle discontinuity. *Nature*, *369*, 474–476. https://doi.org/10.1038/369474a0

Rost, S., Garnero, E. J., Williams, Q., & Manga, M. (2005). Seismological constraints on a possible plume root at the core–mantle boundary. *Nature*, *435*, 666–669. https://doi.org/10.1038/nature03620

Schmandt, B., Jacobsen, S. D., BeckerLiu, T. W. Z., & Dueker, K. G. (2014). Dehydration melting at the top of the lower mantle. *Science*, *344*, 1265–1268. https://doi.org/10.1126/science.1253358

Shen, G., & Lazor, P. (1995). Measurement of melting temperatures of some minerals under lower mantle pressures. *Journal of Geophysical Research*, *100*, 17699–17713. https://doi.org/10.1029/95jb01864

Soubiran, F., & Militzer, B. (2020). Anharmonicity and phase diagram of magnesium oxide in the megabar regime. *Physical Review Letters*, *125*, 175701. https://doi.org/10.1103/physrevlett.125.175701

Stixrude, L., de Koker, N., Sun, N., Mookherjee, M., & Karki, B. B. (2009). Thermodynamics of silicate liquids in the deep Earth. *Earth and Planetary Science Letters*, *278*, 226–232. https://doi.org/10.1016/j.epsl.2008.12.006

Stixrude, L., & Karki, B. (2005). Structure and freezing of MgSiO$_3$ liquid in Earth's lower mantle. *Science*, *310*, 297–299. https://doi.org/10.1126/science.1116952

Stixrude, L., & Lithgow-Bertelloni, C. (2005). Thermodynamics of mantle minerals—I. Physical properties. *Geophysical Journal International*, *162*, 610–632. https://doi.org/10.1111/j.1365-246X.2005.02642.x

Tateno, S., Hirose, K., & Ohishi, Y. (2014). Melting experiments on peridotite to lowermost mantle conditions. *Journal of Geophysical Research: Solid Earth*, *119*, 4684–4694. https://doi.org/10.1002/2013jb010616

Tateno, S., Hirose, K., Sakata, S., Yonemitsu, K., Ozawa, H., Hirata, T., et al. (2018). Melting phase relations and element partitioning in MORB to lowermost mantle conditions. *Journal of Geophysical Research: Solid Earth*, *123*, 5515–5531. https://doi.org/10.1029/2018jb015790

Thorne, M. S., Takeuchi, N., & Shiomi, K. (2019). Melting at the edge of a slab in the deepest mantle. *Geophysical Research Letters*, *46*, 8000–8008. https://doi.org/10.1029/2019gl082493

Tosi, N., Plesa, A.-C., & Breuer, D. (2013). Overturn and evolution of a crystallized magma ocean: A numerical parameter study for Mars. *Journal of Geophysical Research: Planets*, *118*, 1512–1528. https://doi.org/10.1002/jgre.20109

Tsuchida, Y., & Yagi, T. (1989). A new, post-stishovite high-pressure polymorph of silica. *Nature*, *340*, 217–220. https://doi.org/10.1038/340217a0

Usui, Y., & Tsuchiya, T. (2010). Ab initio two-phase molecular dynamics on the melting curve of SiO$_2$. *Journal of Earth Science*, *21*, 801–810. https://doi.org/10.1007/s12583-010-0126-9

Wood, B. J., & Halliday, A. N. (2005). Cooling of the Earth and core formation after the giant impact. *Nature*, *437*, 1345–1348. https://doi.org/10.1038/nature04129

Workman, R. K., & Hart, S. R. (2005). Major and trace element composition of the depleted MORB mantle. *Earth and Planetary Science Letters*, *231*, 53–72. https://doi.org/10.1016/j.epsl.2004.12.005

Zerr, A., & Boehler, R. (1993). Melting of (Mg,Fe)SiO$_3$-perovskite to 625 kilobars: Indication of a high melting temperature in the lower mantle. *Science*, *262*, 553–555. https://doi.org/10.1126/science.262.5133.553

Zhang, L., & Fei, Y. (2008). Melting behavior of (Mg,Fe)O solid solutions at high pressure. *Geophysical Research Letters*, *35*, L13302. https://doi.org/10.1029/2008gl034585